

# Analytical Ultracentrifugation Characterization of Differential Sedimentation Size-Separated Graphene Dispersions

Christopher M. Sims,<sup>1</sup> Jason P. Killgore,<sup>2</sup> Elisabeth Mansfield,<sup>2</sup> Julia R. Downing,<sup>3</sup> Ana C. M. de Moraes,<sup>3</sup> Mark C. Hersam,<sup>3,4,5</sup> and Jeffrey A. Fagan,<sup>1,\*</sup>

1. Materials Science and Engineering Division  
National Institute of Standards and Technology, Gaithersburg, MD USA 20899
2. Applied Chemicals and Materials Division  
National Institute of Standards and Technology, Boulder, CO USA 80305
3. Department of Materials Science and Engineering, Northwestern University, Evanston, IL 60208, USA
4. Department of Chemistry, Northwestern University, Evanston, IL 60208, USA
5. Department of Electrical and Computer Engineering, Northwestern University, Evanston, IL 60208, USA

## ORCID

Christopher M. Sims: 0000-0002-5623-6974

Jason P. Killgore: 0000-0002-8458-6680

Elisabeth Mansfield: 0000-0003-2463-0966

Jeffrey A. Fagan: 0000-0003-1483-5554

Julia R. Downing: No ORCID

Ana C. M. de Moraes: No ORCID

Mark C. Hersam: 0000-0003-4120-1426

*Official contribution of the National Institute of Standards Technology - Not subject to copyright in the United States*

## Abstract

Analytical ultracentrifugation (AUC) is applied to the characterization of as-dispersed graphene nanoplatelet dispersions and differential sedimentation separated daughter dispersions. The liquid-phase characterization of AUC is demonstrated to resolve both the broad sedimentation coefficient distributions of as-dispersed samples, and changes in daughter dispersions determined by a protocol of applied differential sedimentation process steps. Comparison is made to measurements on deposited samples by scanning electron microscopy (SEM) and atomic force microscopy (AFM). The value of AUC to rapidly monitor changes in the sedimentation distribution of each particle population is demonstrated to allow tailoring of the differential sedimentation protocol to produce

---

\* Corresponding Author. email: [Jeffrey.fagan@nist.gov](mailto:Jeffrey.fagan@nist.gov) (Jeffrey A. Fagan)

significantly narrower population distributions. This rapid characterization is particularly important for technologies in which dispersed nanoparticles cannot be removed from a solvent solution for microscopy analysis.

## Introduction

Two-dimensional materials (2D materials), such as graphene, MoS<sub>2</sub>, WS<sub>2</sub> and MXenes, are expected to impact a wide variety of applications. These include a broad range of thin film applications such as semiconductor electronics, barrier films, separation membranes, and sensor devices,[1] but also bulk material applications requiring incorporation into meso- and macroscale composite materials. To enable assembly or incorporation of 2D materials into films or composites, liquid-phase dispersion[2, 3] is commonly utilized, and often necessary for achieving desired properties. The typical goal to liquid-phase dispersion is to exfoliate a multilayer or bulk sample, generating individualized single or few layer sheets of the 2D material within a solvent or resin fluid matrix. Such dispersions are coated on, blended with other components, or processed to generate an integrated composite, achieving generally greater specific properties from the reduced dimension of the exfoliated material. Incorporating liquid-phase processing, however, can be non-trivial.[4, 5] Intrinsic 2D material properties,[6] 2D sheet-level transport phenomena, and fluid properties all depend on the degree of dispersion, the size distribution of the individualized nanoplatelets, and the matrix-influenced liquid-phase interactions between nanoplatelets.[7-9]

Selecting a process for generating individualized and few layer sheets of a 2D material in a liquid-phase dispersion depends on the details of the 2D material synthesis method and chemistry, as well as generally involving considerations of solvent composition, whether to use a dispersant and if so the type, and the desired mass throughput scale of the process.[10] Excluding small throughput processes in which a sub-monolayer of flakes are delaminated from their synthetic support,[3, 11] most dispersion procedures require the input of significant amounts of energy, whether by ball milling, high-shear mixing, or sonication to delaminate individual sheets from multilayer macro or mesoscale powders of the 2D material.[12] These processes are collectively described as liquid-phase exfoliation (LPE), and are known to simultaneously reduce the average flake size and increase polydispersity,[13, 14] especially when the energy input is chosen to maximize mass yield. Notably, conditions that result in an optimal mass yield or other desired dispersion characteristics may not result in a useful, as-produced distribution of dispersed 2D materials, and thus post-dispersion processing is an area of increasing interest.

For many nanoparticle dispersions,[15] and 2D nanomaterials in particular,[16-21] differential sedimentation (DS) is a primary methodology to affect the distribution of particle compositions and sizes in a dispersion and to remove impurity components. In its simplest implementation, DS involves a single stage of

centrifugation of an initially uniform liquid dispersion and separate recovery of the resulting supernatant (liquid) and pellet (solids) phases.[22] In the absence of significant liquid convection during the process, the pellet phase will accumulate a greater fraction of those components of the dispersion that sediment faster (i.e., those components with a larger sedimentation coefficient) than the average rate. In mass ratio the pellet phase will thus be relatively enriched in the faster sedimenting components and the supernatant relatively enriched in slower sedimenting components. As sedimentation speed is related to particle size, aspect ratio, and density, an optimized process can remove aggregates and/or dense impurities or fractionate by particle size. From these daughter populations, additional centrifugation steps can subsequently be applied to preferentially fractionate smaller (larger) components by increasing (decreasing) the time or strength of applied acceleration in a multi-stage cascade. As a methodology, DS is popular due to its simplicity and the broad availability and scalability of appropriate centrifuges.

Difficulties in applying DS include significant effects from variations in geometry across different rotor and centrifuge models, and method-specific details such as the absolute liquid volume in a centrifuge tube or the sequence design of a multi-stage cascade. DS, generally, is only able to completely separate dispersed particles with very different sedimentation coefficients, and thus sedimentation rates, at the same applied acceleration. The primary cause of this low resolution is that both faster and slower sedimenting particles start uniformly distributed throughout the liquid volume, and so the distribution of particles reaching the outer radius to form the pellet will include a fraction of slower (typically smaller) particles that had less distance to travel. Thus, even for materials well-suited for sedimentation-based fractionation (i.e., populations with broad polydispersity in sedimentation rates such as 2D materials), significant overlap in particle distributions collected in adjacent cascade fractions can be expected.[22] Moreover, non-ideal sedimentation effects can make this overlap worse, including non-ideality from particles comprising a significant volume fraction of the sample. Using a common rotor geometry (e.g., fixed angle rotor) also frequently leads to non-ideal sedimentation due to vibrations, interparticle interactions, wall effects, and convection. These confounding factors drive a need for empirical optimization of a DS cascade, which in turn makes the ability to rapidly determine the size, shape, aspect ratio, and density distribution of particles in each separated fraction highly desirable.

For many nanomaterials, including the 2D graphene material explored here, characterization of the size or other polydisperse distribution of a fractionated population is a significant technical challenge. Typical methodologies are based on surface analysis methods including scanning electron microscopy or atomic force microscopy that require deposition from solution and relatively slow measurements to sample enough particles for statistical comparison. Such measurement thus become a bottleneck in any DS protocol optimization. In this work we utilize instead a liquid-phase characterization method, analytical ultracentrifugation (AUC),[23, 24] to

rapidly and directly measure graphene subpopulations generated through DS. Previous literature on AUC characterization of 2D nanomaterials has investigated particle size, shape, and layer number distribution effects.[13, 25] The most common method of AUC measurement, termed a sedimentation velocity experiment, monitors the evolution of an initially spatially uniform concentration distribution of particles in a centrifuge cell through either absorbance or Rayleigh interference optics (*i.e.*, refractive index-based) as a function of radial position during the application of a centrifugal acceleration. Time and spatially varying concentration distributions are then fit (*vide infra*) to extract sedimentation coefficient distributions that, in near-ideal sedimentation conditions such as those used in this work, reflect particle properties such as size, shape, and effective density through known relations.[26] Additional benefits of the AUC technique include minimal absolute sample quantities or concentrations, the ability to preferentially monitor selected components by tuning the wavelength at which the concentration is measured by absorbance, rapid characterization times for determining an entire distribution of particles, and relatively low operator time compared to microscopy methods.

A critical additional aspect of AUC as a characterization method for 2D nanomaterials when applied to exfoliated dispersions is that the AUC characterization is performed with the dispersed nanoparticles *in situ* in their solution environment. This is an important factor for dispersions requiring complex formulations, such as the one used here, or for applications such as a photopolymerizable resin dispersion.[27, 28] In many instances the 2D material may be irretrievable from the dispersion environment, irremovable without changing the distribution or aggregation state, or without including confounding co-components of a mixture. Each of these factors could lead to a 2D material dispersion being amenable to AUC characterization while infeasible for microscopy method analysis.

In this contribution, we demonstrate the utility of the AUC method for enabling evaluation of processing choices in a DS centrifugation cascade. Towards this end, we conduct a DS process on a polydisperse graphene parent dispersion, ending and characterizing the effects of the cascade at different levels of processing. In addition to showing the distinction in daughter samples using AUC measurements necessary for tailoring the separation, we also demonstrate a simple processing variation to increase homogeneity of the resulting populations. This process change, applying additional cycles of centrifugation at either the same or at reduced acceleration to the pellet of a DS cascade, is shown to measurably reduce the polydispersity of the DS cascade-produced subpopulations relative to the common one-step methodology.

## Methods

Certain equipment, instruments, software, or materials, commercial or non-commercial, are identified in this paper in order to specify the experimental procedure adequately. Such identification is not intended to imply

recommendation or endorsement of any product or service by NIST, nor is it intended to imply that the materials or equipment identified are necessarily the best available for the purpose. Except where specified otherwise, uncertainty in this contribution is reported as one standard deviation.

Graphene dispersion parent samples were produced by directly dispersing graphene powder previously prepared by high-shear exfoliation of bulk graphite using ethyl cellulose (Sigma-Aldrich, EC,  $4 \times 10^{-3}$  Pa.s) as a dispersant and stabilizer[29] *via* sonication in ethyl lactate as a solvent. The concentration of this stock graphene dispersion was 25 mg/mL. Additional ethyl lactate (Sigma-Aldrich, (-)-ethyl L-lactate,  $\geq 99.0$  %) was used as received for dilution operations and resuspension of pellet fractions from DS steps. The density and viscosity of ethyl lactate at 20.00 °C were measured to be 1034.449 kg/m<sup>3</sup> and 2.798 mPa s, respectively, using an Anton-Paar DMA 5000 M - Lovis 2000 ME densimeter-microviscometer.

Differential sedimentation (DS) experiments were primarily conducted in a benchtop microcentrifuge (Thermo Scientific Sorvall Legend Micro 21) as an instrument considered representative of widely available equipment. The instrument rotor model number was 7500 3424, which can accept 24 x 2 mL microcentrifuge tubes. Capped microcentrifuge tubes of 1.5 mL nominal volume (various suppliers) were used for DS cascades. The geometry of such centrifuge tubes (shorter length) reduces the applied maximum acceleration from the instrument reading by a factor of  $\approx 15$  %. Nominal accelerations from the instrument reading were (500, 1200, 2400, 5000, 8000, 12000 and 17000) x G ( $G = 9.81 \text{ m/s}^2$ ) for steps 1 - 7. Safety note: centrifuge tubes should be checked for chemical compatibility and speed rating before use. Schematics and additional descriptions of the differential sedimentation schemes used in this contribution are presented in the Results and Discussion section. The concentration of the parent graphene dispersion for DS was diluted to 2.5 mg/mL so that successful separation of the pellet and supernatant phases could be observed visually. To increase mass throughput and enable longer cascades of fractionation, however, the parent cascade was started with 6 replicates. The initial volume of each aliquot before centrifugation was 1600  $\mu\text{L}$ . Centrifugation time at each step was 1 h 40 min divided into two equal parts. At the conclusion of the first time period, the centrifuge tubes were rotated 180° around their central axis such that the outer radius and inner radius of the tube change positions; this rotation vastly reduces deposition of the pellet phase on the upper wall region of the centrifuge tube and improves fidelity of the DS separation. Post-centrifugation, 1500  $\mu\text{L}$  was removed as the supernatant phase, and 100  $\mu\text{L}$  was retained as the pellet phase; the actual observed pellet volume was estimated as  $\approx (80 \text{ to } 85) \mu\text{L}$  for most cascade steps; a greater extraction fidelity is not practical at this volume scale of operation. Pellet phases were recovered by dilution and agitation with fresh solvent. At each stage, the resulting supernatant and pellet samples from all replicates were combined before sampling of aliquots for characterization and redistribution into new centrifuge tubes for additional DS

steps. Additional fresh solvent was added to account for the volume removed in sampling for AUC and other measurements.

Analytical ultracentrifugation (AUC) was conducted in a Beckman-Coulter XL-I analytical ultracentrifuge with an An-50 Ti rotor and 12 mm optical pathlength aluminum cells with sapphire windows and custom cut polytetrafluoroethylene (PTFE) gaskets. PTFE gaskets (between the centerpiece and windows) provide broad chemical compatibility (avoiding solvent swelling of the gaskets and leakage) for many non-aqueous fluids including ethyl lactate. For all measurements, the rotor temperature was set to 20.0 °C, validated within the instrument accuracy specification of  $\pm 0.5$  °C by external calibration,[30] and samples were equilibrated in the instrument for a minimum of 1.5 h before starting experiments. Different rotation rates were applied depending on the sample to optimize data collection for the primary components (daughter fractions) or to enable reasonable sampling of the entire population (parent distribution). For the parent dispersion, rates of 850 rad/s (8 kRPM) and 2100 rad/s (20 kRPM) were used in different experiments to ensure observation of both the slowest and fastest components. Daughter fractions expected to contain larger particles, *e.g.*, P1 – P4, were measured at rates as slow as 315 rad/s (3 kRPM). For daughter fractions expected to contain smaller particles, rotation rates up to 1810 rad/s (17.3 kRPM) were applied to fully and distinctly sediment all dispersed particles. Gravitational sweep methods could also have been used,[31] however, daughter distributions are well-observed at the fixed rotation rates. Radial absorbance scans were measured at 304 nm, with different dilution factors of neat solvent applied to each sample to target an initial absorbance of  $\approx 0.8$  across the 12 mm cell. For the parent dispersion, the dilution factor was 2000:1, with the large polydispersity resulting in significant noise in the distribution due to the dilution of the total signal. The typical sample and reference volumes in each cell were  $\approx 400$   $\mu$ L.

Analysis of the recorded radial absorbance profiles as a function of time was conducted using the numerical fitting software SEDFIT v. 16.1c.[32, 33] Sedimentation was fit for most samples using the  $ls-g^*(s)$  model due to observed fast sedimentation rates, which implied minimal contributions from diffusion in the concentration profiles. The  $c(s)$  model, which includes contributions from diffusion in the data fit, was applied in parallel for those fractions containing the smallest particles but was not found to significantly affect the fit and thus are not reported here. Typical parameters for the  $ls-g^*(s)$  model were an  $s$ -value range of (1 to 5000) sv ( $sv \equiv 1 \cdot 10^{-13}$  s) linearly discretized with 501 values, and a regularization of 0.95, although these parameters were adjusted for different fractions to account for the shift in the observed distributions. The meniscus and noise were fit for each experiment and agreed well with the apparent positions in the data.

Scanning electron microscopy (SEM) and atomic force microscopy (AFM) were conducted on diluted and dried aliquots of parent dispersion and daughter fractions. Silicon wafers were cleaned and then placed in an ultraviolet (UV) - ozone cleaner for 20 min. The wafer was placed on a hot plate at 110 °C, and 1  $\mu$ L of a 1:10

dilution in ethanol of the stock solution was deposited onto the heated wafer. SEM analysis was performed using an in-lens detector on a Zeiss Gemini scanning electron microscope at 5 keV. SEM particle size analysis was completed by measuring the longest dimension in ImageJ on a calibrated image. AFM Analysis was conducted using a Cypher (Asylum Research, USA) instrument operated in amplitude modulated intermittent contact mode (*i.e.*, tapping mode). For each dispersion 5 scans with 20  $\mu\text{m}$  x 20  $\mu\text{m}$  scan area were performed. Images were acquired in a net repulsive force regime, with 1024x1024 pixels (*i.e.*,  $\approx$  20 nm pixel size) and a 0.1 Hz imaging rate. The slow imaging rate and high pixel resolution ensure well resolved topographic characterization of the individual particles. Particle analysis was carried out by adapting a recent method under consideration by Versailles Project on Advanced Materials and Standards (VAMAS) for characterizing the distribution of lateral sizes and thickness of few-layer graphene and related 2D materials.[34] Briefly, after identifying a particle of interest, the long and short axis dimensions are measured at the base and top plane of the particle to determine length and width lateral dimensions. Thickness is measured along the fast scan axis of the AFM at three locations per particle. Approximate particle volumes were calculated as the product of the determined particle length, width, and thickness. Measurements were continued until 20 suitable particles were characterized per dispersion (except for P3PS where 16 suitable particles were found in the datasets). Discriminating primary particles from agglomerates and dispersant clusters was particularly challenging. To aid in identification, AFM height, phase and amplitude error were used simultaneously to identify graphene. Typically, graphene exhibited minimal phase contrast compared to substrate, whereas the dispersant showed a much lower phase than the substrate. For comparison purposes, a separate automated particle analysis methodology was also performed using tools provided in the AFM's native software suite. Automatic analysis was performed with a 5 nm height threshold for identifying particle perimeters from the surface.

## Results and Discussion

Dispersed 2D nanomaterials are of particular interest for fractionation technologies, as equipartition of energy[14] in any dispersion process leads to significant polydispersity in such dispersions, and factors such as the lateral sheet size and aspect ratio affect the suitability of the materials for applications. For the graphene dispersion used in this contribution SEM images shown in Figures 1A and 1B display objects varying in size by at least 40-fold in areal projection. AUC data and the best fit sedimentation coefficient distribution (Figure 1C) display a similar range of particle variation.

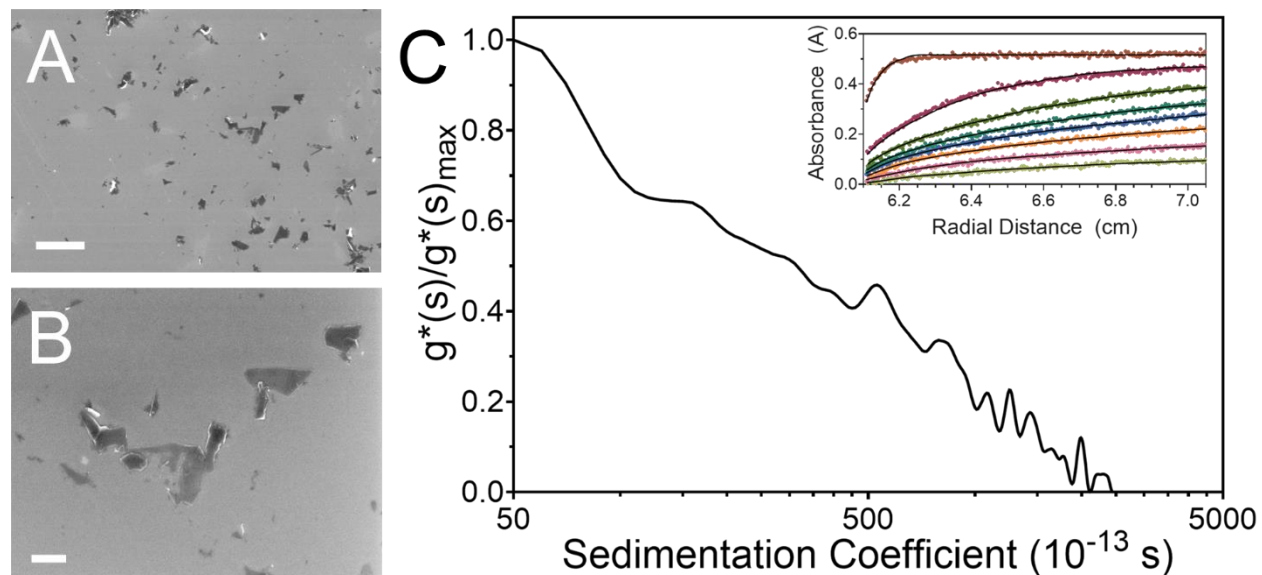


**Figure 1.** Characterization of the graphene parent dispersion in ethyl lactate. **A, B.** SEM images of a dropcast aliquot of the parent dispersion demonstrating a wide range of particle sizes with both extended and compact lateral shapes. Scale bar in **A** is 2  $\mu\text{m}$ ; the scale bar in **B** is 400 nm. **C.** Best fit sedimentation coefficient distribution to the observed concentration distributions in the AUC experiment for the parent dispersion. The inset shows selected radial absorbance profiles (304 nm) at 9-minute increments (every 3<sup>rd</sup> scan) from a representative AUC measurement of the parent sample at 838 rad/s (8 kRPM) at 20.0 °C in ethyl lactate solvent. The stretched concentration boundary in the inset and the broad distribution of the sedimentation coefficients are consistent with the expected presence of significant variation in dispersed graphene sizes, layer numbers, and flake shapes.

In ideal sedimentation, the sedimentation rate per applied acceleration, defined as the sedimentation coefficient,  $s$ , can be described by the Svedberg equation.[23, 24]

$$s = \frac{V_{\text{particle}} (\rho_{\text{particle}} - \rho_{\text{solvent}})}{f} = \frac{V_{\text{particle}} (\rho_{\text{particle}} - \rho_{\text{solvent}})}{6\pi\mu a^* f / f_0} \quad (1)$$

In Equation 1,  $V_{\text{particle}}$  is the particle volume,  $\rho_{\text{particle}}$  and  $\rho_{\text{solvent}}$  are the particle and solvent densities, and  $f$  is the friction coefficient. For simplification, the friction coefficient is typically specified by the shape-dependent reduced friction coefficient,  $f/f_0$ , with  $f_0 \equiv 6\pi\mu a$ , in which  $\mu$  is the solvent viscosity, and  $a$  is the radius of a sphere of equivalent mass and density. For a platelet geometry,  $f/f_0$  increases for decreasing height to diameter ( $h/d$ ) ratios from a value of 1 for an ideal sphere without hydration to  $\approx 5$  for a 2D plate with  $h/d = 0.001$ . [25] Since the range of observed  $s$  is much greater than this variation, it is clear that the parent distribution in this work contains a wide variety of particle thicknesses, lateral sizes, and aspect ratios, as expected for a population generated by ultrasonication.

Previously, Walter *et al.*[25] reported the development of density and hydrodynamic parameters for graphene oxide nanoplatelets in an aqueous dispersion. As a related material and given similar sedimentation rates and signal concentrations, we analyze our ethyl cellulose dispersed graphene in ethyl lactate using similar

tools and assuming ideal sedimentation.[35] Followingly, we assume that the measured extinction signal is solely absorbance based, particle crumpling is minor, and particle rotation is sufficient for the friction coefficient to be independent of sedimentation rate.[25, 36] Purely for demonstrational conversion to number distributions, we assume a representational particle density (including dispersant) of  $1500 \text{ kg/m}^3$  and an average hydrodynamic thickness of the 2D sheets of 8 nm; direct evaluation of these parameters (which are distributions in this sample) is beyond the scope of this contribution but potential methods for calibration are discussed later. As in Walter *et al.*[25] the assignment of measured extinction entirely to absorbance matched well with experimental observations, especially since as-measured populations were dilute and negligible multiple scattering was anticipated. Calculated assignment of some signal to scattering would imply lower number concentrations of high  $s$ -value particles due to their presumably larger size. Importantly, precise calibration of  $s$ -value to size and shape are not needed for the direct utilization of AUC for the rapid evaluation of DS or other processing-separated populations.[37]

Although DS cascade methods are the focus of this contribution, several different types of centrifugation methods can be considered to reduce the polydispersity of a nanomaterial dispersion.[38] These alternatively include rate-zonal methods[39-41] in which the nanomaterial races through an initially particle free medium, and density gradient ultracentrifugation methods[42-45] in which the individual particles are driven to positions of equal buoyancy in a spatial gradient with very strong applied acceleration. Since DS methods are capable of greater mass throughput while avoiding the costs of density gradient media and more sophisticated centrifuges, they are broadly utilized for lab-scale separations. The simplest DS method that collects both the pelleted and supernatant materials as daughter fractions is shown schematically in Figure 2. In this simple cascade, an aliquot of dispersion is centrifuged for a period of time at a set acceleration to split the dispersed mass between a pellet phase of sedimented particles and a supernatant containing all the particles not reaching the pellet. The supernatant is then extracted to a liquid level just shy of entraining the pellet mass, generating two separated fractions,  $P_i$  and  $S_i$  for the  $i^{\text{th}}$  pellet and supernatant phase, respectively. For non-aggregating particles, the pellet can be redispersed *via* agitation with fresh solvent, and either the supernatant or pellet fraction subjected to an  $i + 1$  DS step.

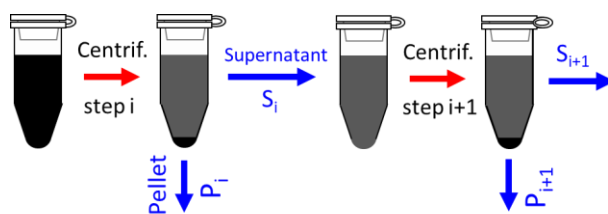


**Figure 2.** Schematic of a typical DS centrifugation cascade. At each step (step  $i$ ), an initially uniform dispersion is centrifuged with the goal of selectively partitioning particles with greater sedimentation coefficients into a pellet phase that can then be physically separated. In a multistage process, the collected supernatant is diluted and then centrifuged at a greater acceleration (step  $i+1$ ) to fractionate progressively more slowly sedimenting components.

The AUC results of such a simple serial DS cascade for the graphene dispersion of Figure 1 are shown in Figure 3A. After seven stages of a DS cascade, increasing the applied acceleration by a factor of approximately two (steps 1 through 4) and then  $\approx 1.5$  (steps 5 through 7) per step (excepting the final step, at which the maximum acceleration was applied), the initial, broadly decaying, sedimentation coefficient distribution is clearly fractionated into seven well-differentiated populations with distinct and progressively shifting maxima. Furthermore, the values of the distribution maxima scale closely with the increases in the applied acceleration, as shown in Figure 3B, demonstrating the selection power of even a simple DS cascade. A re-scaled version of Figure 3 designed to report the relative concentrations of the fractions to each other is provided in the SI as Figure S2. It is important to note that the exact distributions fractionated into the supernatant and pellet will depend on particle and solvent properties (*e.g.*, densities and viscosities) and the rotor and centrifuge tube geometries and  $k$ -factors;<sup>[22]</sup> however, the distributions measured below reflect a commonly accessible rotor and tube geometry and thus are instructive of the relative fractionations that can be accomplished.

Addressing the use of AUC to measure such distributions, an increased measurement precision of daughter fractions is immediately noticeable due to the reduction in noise in the plotted distributions compared to the parent sample. While the smoothness of the curves is affected by the regularization applied in data analysis, the relative comparison to the parent distribution is still valid, and the improvement can be predominantly attributed to the concentration of the measured signal into narrowed sedimentation coefficient ranges. This increased precision allows observation of distribution tails, in particular to the lesser sedimentation coefficient range, that overlap for all the daughter populations. If coarser separations or an even more polydisperse parent sample were under investigation, the use of a gravitational sweep AUC methodology<sup>[31]</sup> could provide such details as well, but most likely at a lesser resolution than the methodology used here.

In comparison to other techniques, the distributions in Figure 3A were determined from numerical fits to the time-dependent radial absorbance profiles, and are thus closely reflective of particle mass distributions, rather than number distributions directly determined *via* counting methods. Using the mass-scaling for spherical particles as an example, in the presence of perfectly accurate particle counting, an equal mass of  $s = 100$  sv and  $s = 500$  sv ( $sv \equiv 1 \cdot 10^{-13}$  s) particles would reflect an approximately 12-fold difference in number concentration, potentially obscuring the primary shifts in the distribution.

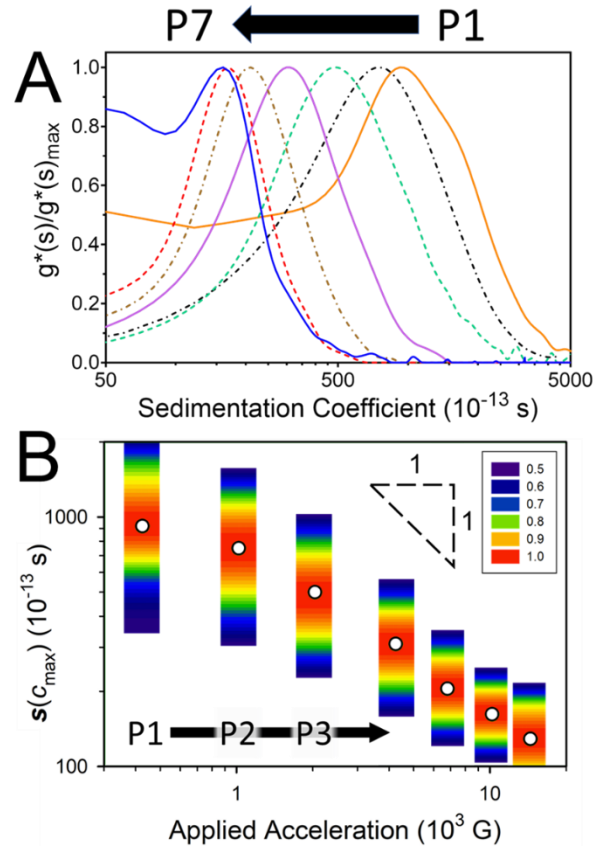


**Figure 3. A.** Scaled sedimentation coefficient distributions for  $P_i$  DS cascade samples as analyzed with the  $1s-g^*(s)$  model. The separation cascade successfully fractionates daughter populations with significantly different average and peak values. Distribution tails, in particular to lesser sedimentation coefficient values, are expected due to the geometry and restrictions for practical extraction of fractions in the separation (see text). **B.** Peak sedimentation coefficient (points) and contour plot distributions for each  $P_i$  fraction as a function of the applied acceleration at the maximum radius. Contours show the width of the distribution to half of the maximum value. The scaling of the achieved separation is less than the slope of -1 on the log-log scale expected for ideal centrifugal separations due to the differential separation setup and centrifuge tube geometry.

Using AUC as a primary characterization method, we now address the question as to whether nominal modifications of the DS cascade can be utilized to achieve narrowed sedimentation coefficient distributions. Three of the primary sources of polydispersity in a DS separated population are: 1) the undesired sedimentation of lesser  $s$ -value components that happen to reside nearer the outer radius due to the uniform initial spatial distribution; 2) the undesired retention in an ancestor supernatant phase of greater  $s$ -value components due to wall effects; and 3) collection inefficiency in separating the pellet and supernatant. The magnitude of the first two factors will depend significantly on the geometry of the DS centrifugation, and the third on the precision of the fractionation. In Figure 3A, the presence of lesser  $s$ -value tails is due to effects one and three. Fortunately, the effects of these sources of polydispersity propagation can also be sequentially addressed by the addition of a DS step. A schematic for the addition of such steps into a DS cascade is shown in Figure 4. To reduce the presence

of lesser  $s$ -value components, a second DS fractionation replicating the DS step that produced the pellet fraction is conducted after dilution and redispersion of the pellet phase to its original volume. This step, labelled with the number 2 in Figure 4, should reduce the fraction of lesser  $s$ -value components that reach the pellet by at least the dilution factor of the pellet, whereas the large majority of targeted components near the distribution maxima will continue to reach the pellet as, by inference from the first stage separation, they previously did so. Reduction in the absolute total concentration of particles during the repeat step will also typically reduce effects from non-ideal sedimentation phenomenon including both kinetic (flow entrainment) and thermodynamic (interparticle interaction) sources.[24, 46] Such effects might be more prevalent in 2D material systems due to the extended nature of the particles, but dilution is not necessarily a panacea for all particle and solvent systems, and care should be observed for separations in highly charged systems, or systems with low ionic strength media.[23] Although not an issue for the particle, solvent, and dispersant system used in this contribution, when applying differential sedimentation to samples with lesser stability to aggregation or readily displaced dispersant, addition of more dispersant or energy may also be necessary with dilution of the pellet to avoid formation and measurement of aggregates.

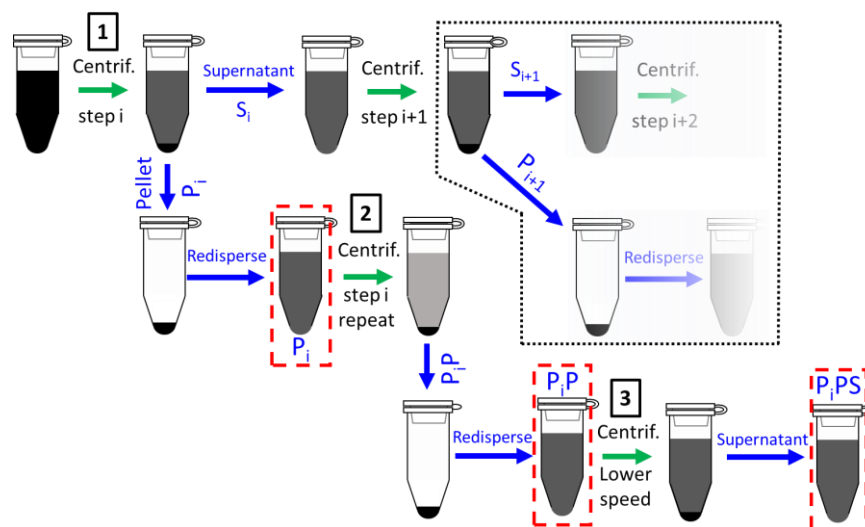


**Figure 4.** Example of a revised DS cascade design incorporating additional centrifugation steps to narrow the sedimentation coefficient distributions of the  $i^{\text{th}}$  fraction. The repeated centrifugation step (2) is intended to reduce in  $P_iP$  the population of lesser sedimentation coefficient particles in pellet  $P_i$ ; the lower speed centrifugation (3) of  $P_iP$  is intended to remove those particles with the greatest sedimentation coefficients, typically present due to non-ideality in fractionation of  $i-1$  step populations. Analysis by AUC occurs at the steps highlighted by the dashed (red) boxes.

The results of including a repeated centrifugation step, as shown schematically in Figure 4, on the AUC-determined sedimentation coefficient distributions are reported in Figure 5. The immediate and obvious observation in the comparison of Figure 3 and Figure 5 is the dramatic reduction in observation of lesser  $s$ -value

components in every P<sub>i</sub>P sample. Such a reduction is particularly important for DS fractionations designed to reduce particle number-based size distribution widths as a quadratic (2D plate) or cubic (sphere) dependency on the increase in number of particles for a fixed mass with decreasing particle size can readily convert lesser *s*-value absorbance tails to dominant particle number peaks. Greater *s*-value tails are suppressed in particle number distributions for the same reason. An example of converting the absorbance-weighted distributions of Figure 3A to number-weighted distribution is shown in the SI in Figure S3.

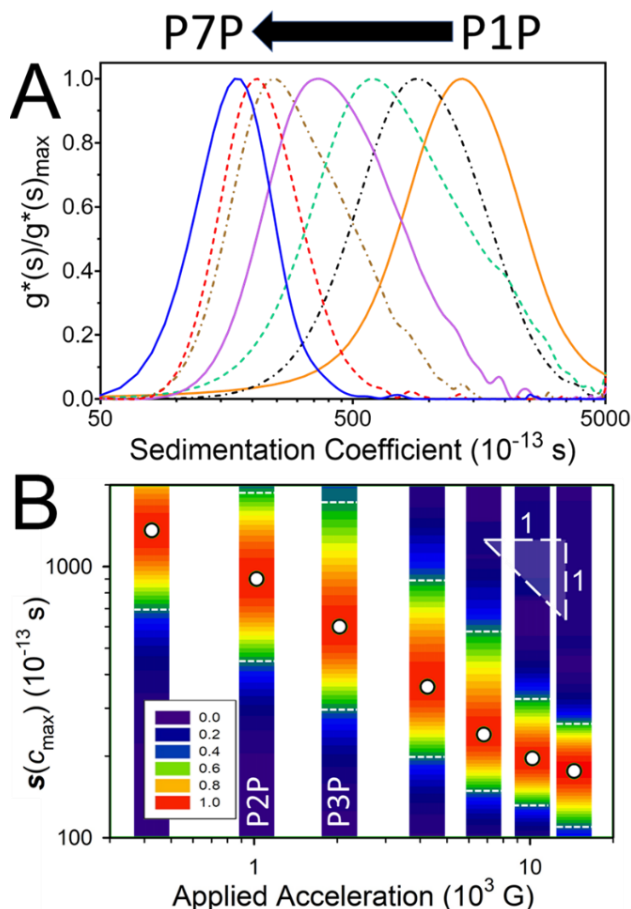


**Figure 5. A.** Scaled sedimentation coefficient distributions for P<sub>i</sub>P DS cascade samples as analyzed with the  $1s-g^*(s)$  model. The addition of the repeat step is observed to significantly reduce the concentration of slowly sedimenting particles (small *s*-values) compared to the single DS cascade (Figure 3). **B.** Peak sedimentation coefficient (points) and contour plot distributions for each P<sub>i</sub>P fraction as a function of the applied acceleration at the maximum radius. White dashes show the width at half the max value. The scaling of the achieved separation is significantly closer to a slope of -1 than the P<sub>i</sub> samples.

The reduction in the sedimentation coefficient distribution width for P<sub>i</sub>P samples as measured by AUC *in situ* is direct and clear. Such distributions can be evaluated qualitatively and quantitatively directly as the solution and measurement conditions can be held consistent for all the samples, and without uncertainty induced by inherently distinct process steps such as deposition. Performing a least-squares fit through the peak values of

fractions P1 – P6 and P1P – P6P in Figures 3B and 5B, the best fit scaling slopes are for the acceleration to the power of -0.686 and -0.735, respectively, indicating an overall improvement in the apparent ideality of the achieved separation. While the reduction in distribution width from addition of a second step is impressive, such distributions still may not be as narrow as desired for intrinsic material characterization. With regards to DS process development, targeting a yet narrower distribution could be achieved by either reducing the acceleration applied in the second step, nominally fractionating a greater percentage of lesser  $s$ -value components to the supernatant at the cost of mass throughput, or addition of a third (overall) DS step. For demonstration purposes, we choose the latter option and perform an additional DS centrifugation at a reduced applied acceleration and collecting the supernatant as the desired fraction. By applying a DS step at reduced acceleration, selective fractionation of greater  $s$ -value particles to the pellet should be achieved, narrowing the distribution remaining in the targeted supernatant. For simplicity, we chose a reduced acceleration equal to that of the  $i-1$  step in the initial DS cascade. Quantifying the narrowing of the (signal-weighted) distribution, the full width at half maximum (FWHM) values are decreased on average by 18 % from a single DS step separation. A more useful metric for specifying properties, however, could be the fractional absorbance contributed by species with an  $s$ -value within a factor of two of the peak; this metric on average increases by 14 % with multistage centrifugation. These metrics are reported in Table 1 and were directly calculated from the determined sedimentation coefficient distributions. A graphical comparison is presented in the SI as Figure S5. For the reasons noted above, conversion of signal (absorbance) weighted distributions to number distributions using a geometric model would likely amplify the narrowing of the distributions due to the scaling of particle number and mass with particle size.

A graphical comparison of the effect of including the second additional DS step (step 3 in Figure 4) for a representative fraction, P4 → P4P → P4PS, is shown in Figure 6A. Figure 6B shows the comparison of the peak values and concentration contours similar to Figures 3B and 5B for the P<sub>i</sub>PS fractions. Due to the preferential removal of the fastest sedimenting material, P<sub>i</sub>PS distributions are narrower than P<sub>i</sub>P distributions. The slope of the center populations (scaling by the P<sub>i</sub>P acceleration) approaches the anticipated ideal scaling. Sedimentation coefficient distributions for the remaining P<sub>i</sub>PS fractions are presented in the SI. A comparison between  $c(s)$  and  $ls-g^*(s)$  model analysis of the AUC data for fraction P6PS, showing negligible difference in the determined  $s$ -value distributions, is also provided in the SI as Figure S6.

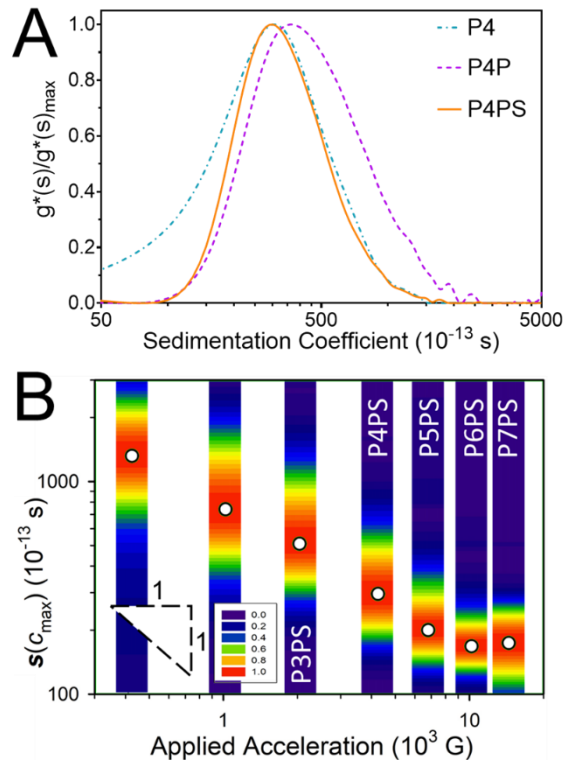


**Figure 6. A.** Scaled sedimentation coefficient distributions for P4 (dot-dash), P4P (dash) and P4PS (solid line) fractions from an example DS cascade as measured by AUC and analyzed with the  $ls-g^*(s)$  model. The reduced acceleration DS step was conducted at the acceleration used to originally fractionate P3. When presented for a single  $i^{th}$  fraction, the effect of the additional centrifugation steps on the width of the population distribution due to the removal of both small and large  $s$ -value components is clear. **B.** Peak sedimentation coefficient (points) and contour plot distributions for each  $P_iPS$  fraction as a function of the applied acceleration for  $P_iP$  at the maximum radius. White dashes show the width at half the max value. The scaling slope of the achieved separation  $\approx -0.8$ , close to the ideal slope of  $-1$ , for P1PS – P6PS.

**Table 1:** Metrics for distributions as a function of DS step

Step #	FWHM / $s(C_{max})$			Fraction of abs. within $\frac{1}{2} s(C_{max}) < s < 2 s(C_{max})$		
	$P_i$	$P_iP$	$P_iPS$	$P_i$	$P_iP$	$P_iPS$
1	$1852 \pm 57$	$1760 \pm 57$	$1653 \pm 42$	$.566 \pm .015$	$.722 \pm .011$	$.757 \pm .007$
2	$1285 \pm 42$	$1352 \pm 42$	$1199 \pm 28$	$.642 \pm .015$	$.695 \pm .013$	$.666 \pm .010$
3	$830 \pm 35$	$1216 \pm 35$	$762 \pm 42$	$.613 \pm .020$	$.477 \pm .013$	$.634 \pm .018$
4	$419 \pm 14$	$619 \pm 28$	$359 \pm 11$	$.713 \pm .012$	$.616 \pm .017$	$.742 \pm .008$
5	$240 \pm 7$	$382 \pm 14$	$187 \pm 6$	$.760 \pm .008$	$.599 \pm .014$	$.820 \pm .005$
6	$149 \pm 3$	$173 \pm 6$	$102 \pm 3$	$.784 \pm .004$	$.873 \pm .005$	$.923 \pm .002$
7	$204 \pm 4$	$141 \pm 3$	$138 \pm 3$	$.736 \pm .008$	$.921 \pm .003$	$.938 \pm .002$

- Uncertainty in FWHM is estimated as the square root of two bin widths used in the numerical fitting of the sedimentation coefficient distribution.
- Uncertainty estimated from the standard deviation of values comprising all combinations of  $\pm 1$  bin on both sides of the fit distribution.

Although the comparison of sedimentation coefficient distributions, and conversions to absolute sizes *via* known material properties should be sufficient for many implementations, precise characterization of the particle size and aspect ratio distributions from the AUC data may still require surface deposition and direct particle imaging methods to specifically tailor the conversion calculations. Multiple factors contribute to the sedimentation coefficient of a 2D material particle,[25] and the combination of factors that result in a specific *s*-value can be non-unique. Evaluating the buoyant density distribution (but without solvent contributions) of the particles with AUC[47, 48] is one potential manner to address this issue, as it yields data for deconvolving density and shape effects, but could not be applied here due to the unavailability of fully deuterated ethyl lactate from a commercial source. Most likely such an experiment would enable observation of layer number variation, which is expected to impact the effective density through the differences in contributions of dispersant and particle density, more than observation of a distribution of particle friction coefficients, as can be achieved for less polydisperse nanomaterials.[47, 48] Separately, spectroscopic methods have been advanced[49-51] based on the size and layer dependent properties to characterize dispersed separated materials, and depending on the 2D material these may provide an alternative reference for calibrating separated dispersion.

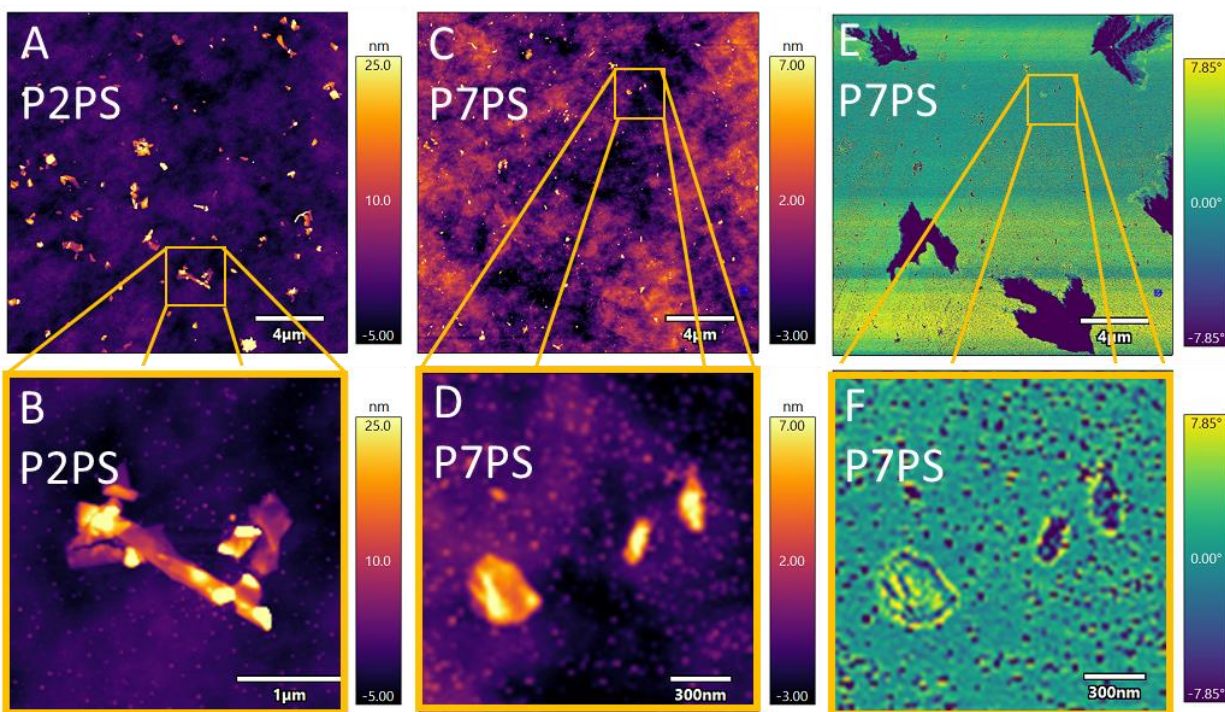


**Figure 7. A-D.** Representative AFM maps of particles observed after deposition from fractions P2PS and P7PS at two different field of view scales. The height images resolve particles showing clear differences in particle size and concentration. **E-F.** Phase maps indicate mechanical and chemical differences in surface that can be used to differentiate graphene particles from dispersants and dispersant aggregates.

For comparison in this effort we report representative scans, observed log volume distributions, and particle thickness *versus* lateral size scatterplots as determined *via* AFM for selected fractions in Figure 7 and Figure 8. Figures 7A and 7C show representative scans of the P2PS and P7PS dispersions (scans for additional dispersions in SI). Clear differences in particle size and concentration are apparent between the images, with obviously decreasing particle size upon increased parent sedimentation. Figure 7B shows a zoomed region of the P2PS dispersion, highlighting an aggregated particle that did not meet the subjective criteria for statistical inclusion. Figure 7D shows a zoomed region of the P7PS dispersion. The smaller particles in the later cascades present a particular challenge for microscopy-based characterization because their dimensions are similar to or approach those of released dispersants or other contaminants present. Some discrimination is possible through the AFM measurement phase channel, which is proportional to the ratio of dissipated and stored energy in the tip sample interaction (akin to loss tangent); this data is shown in Figure 7E and Figure 7F. For quantification of distributions, the mechanical contrast from the phase channel was used to differentiate dispersant (lower phase than substrate) from graphene (similar phase as substrate), even for features otherwise similar in dimension. Figure 8A reports the particle thickness *versus* mean lateral dimension for each of the daughter fractions as determined through the manual particle measurement method. The plot shows distinct populations based on particle geometry from the DS fractionation. Figure 8B reports the particle volume distributions of the same measured particles from the DS daughter dispersions. The analysis finds that the mean particle volume reduces by approximately 1 order of magnitude from P1PS to P7PS, consistent with the reduction in sedimentation coefficient for the same dispersions from AUC in Figure 6B. As expected from the physics of sedimentation, selection of particles into specific fractions occurs through a combination of thickness and lateral dimension. Higher order interpretations considering particle aspect ratio are also possible from the raw data. The variation in the populations generally tightened at later steps in the cascade as well, likely from a combination of selective removal in earlier steps, and in the number of steps at which outlier particles had the possibility of being diverted.

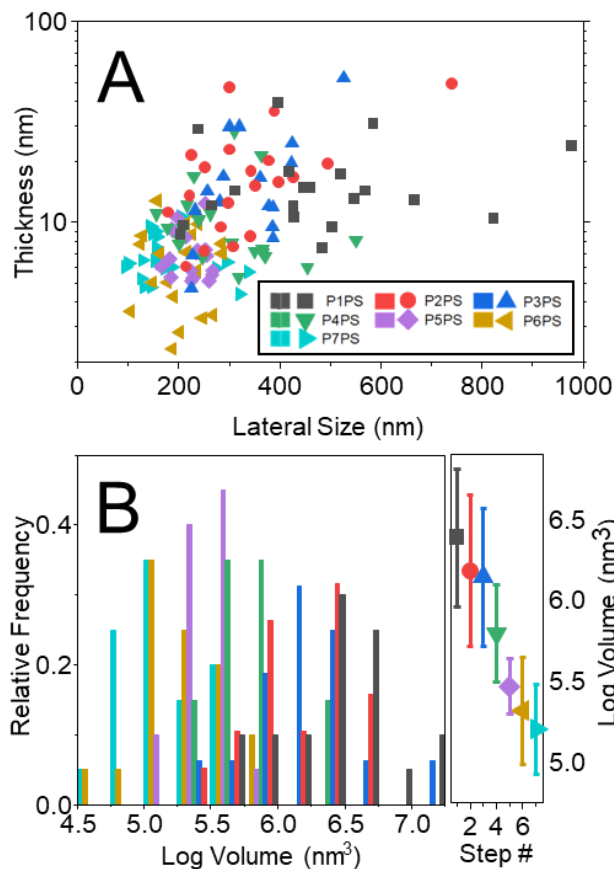


**Figure 8. A.** Scatterplot of particle height *versus* lateral dimension measurements from individual deposited particles in P<sub>i</sub>PS daughter fractions. Note that the legend is consistent across both panels. **B.** Statistical comparison of observed log volume of identified graphene particle size frequency for P<sub>i</sub>PS fractions. In the left side the data points in panel A are reported as a histogram of the observed log volume for each P<sub>i</sub>PS fraction. Although changes in the volume distribution are readily observed, the nominal overlap and coarse binning of the distributions required with small particle counts significantly reduce the feedback efficiency if the data is used for DS cascade modification and optimization relative to the use of AUC. The right-hand panel plots the mean values and distribution widths for each fraction for a gaussian fit (of log volume) to the histogram data; these decrease with each DS processing step.

Comparing the AFM and AUC, clear differences are observed in the subjectivity and effort required to analyze distributed populations coming from a complex solution environment. The AFM results required considerable user time and subjective interpretation to achieve meaningful statistical analysis. AUC analysis in contrast required limited assumptions, specifically that sedimentation was dominant over diffusion for these samples (see Figure S6), and that the dilution to a similar dilute absorbance for measurement of each fraction was sufficient for non-ideality effects to be minimal (tested). Although AFM software often provides automated particle analysis as a built-in feature, for application to the graphene dispersion of this work such tools were only found to poorly characterize the primary particles as distinguished from deposition artifacts or dispersant particle.

SI Figure S9 provides a comparison of the results of manual and automated analysis on the P2PS dispersion and P6PS dispersions. In this comparison the automated analysis was selecting particles based on height thresholding and other geometric criteria. However, because the automated method only considers a single channel (*i.e.*, height), it is not simultaneously combining height and phase information to improve confidence in identifying real graphene particles from artifacts such as dispersant clusters. Similarly, the automated analysis had only limited means for excluding aggregate particles, which appear to be deposition artifacts as the separation selectivity and AUC results both imply that they were unlikely to have existed while still in liquid dispersion. A test for solution aggregation could include addition of sonication after the centrifugation steps to disassociate any loosely bound aggregates, but with a hazard that the high energy input could conceivably fracture real larger particles. It is important to note that while such challenges may not be present when operating with pristine samples without dispersants, or can be overcome through heroic efforts, neither case is feasible for the tuning of multiple parameters in a multistep process, *e.g.*, engineering a DS cascade, or possible with all complex sample environments. Resultingly, the automated analysis is found to report un-physically broad distributions that include both small side tails, dominated by incorrect counting of small dispersant particles, and upper tails dominated by counting of aggregates.

## Conclusions

Analytical ultracentrifugation is demonstrated to precisely measure the achieved fractionation of 2D graphene dispersions separated by differential sedimentation. Moreover, the effects of a multiple DS step cascade were shown to be quantitatively compared both across a cascade and in refinement of separated populations, providing a methodology to rapidly compare and iterate processing schema. These comparisons include contributions from tails of distributions that can be observed because of the separating and measuring nature of the AUC method and the number of particles effectively sampled in the measurement volume. Comparative results from AFM measurements were in good qualitative agreement with the AUC results. However, artifacts generated by deposition are particularly difficult for AFM measurements on 2D material systems with robust dispersants or unusual solvents, such as the one used here, and quantitative attribution of *s*-values to particular sizes and shapes of particles was not feasible. In the future, using well-defined materials, quantitative determination of populations from sedimentation coefficients across a broad range of particle lateral sizes, aspect ratios, and thickness distributions may be directly possible through hydrodynamic and force balance relations. In comparison, the effects of the solvent and dispersant choice were minimized in the AUC data due to the significant dilution before measurement and tailorable nature of the observed sedimentation coefficient range in measurement. The flexible liquid-phase format of AUC should be broadly applicable for analysis of other 2D

nanomaterial dispersions in complex dispersions and to the characterization and engineering of other fractionation methods[40, 52, 53] beyond DS cascades.

## Acknowledgement

CMS, JPK, EM, and JAF were supported by internal National Institute of Standards and Technology funds. Graphene powder and dispersion production (JRD, ACMdM, MCH) was supported by the U.S. Department of Commerce, National Institute of Standards and Technology (Award 70NANB19H005) as part of the Center for Hierarchical Materials Design (CHiMaD) and the National Science Foundation Future Manufacturing Program (NSF CMMI-2037026).

## Supplemental Information

The Supplemental Information contains additional absorbance, SEM and AFM data from characterization of the parent and daughter DS cascade samples, as well as comparisons of AUC distributions recalculated to display relative concentrations of fractions by mass, representative conversion of some distributions to number weighted distributions, and the comparison of the effect of DS processing on the measured distribution for each major daughter fraction.

## References

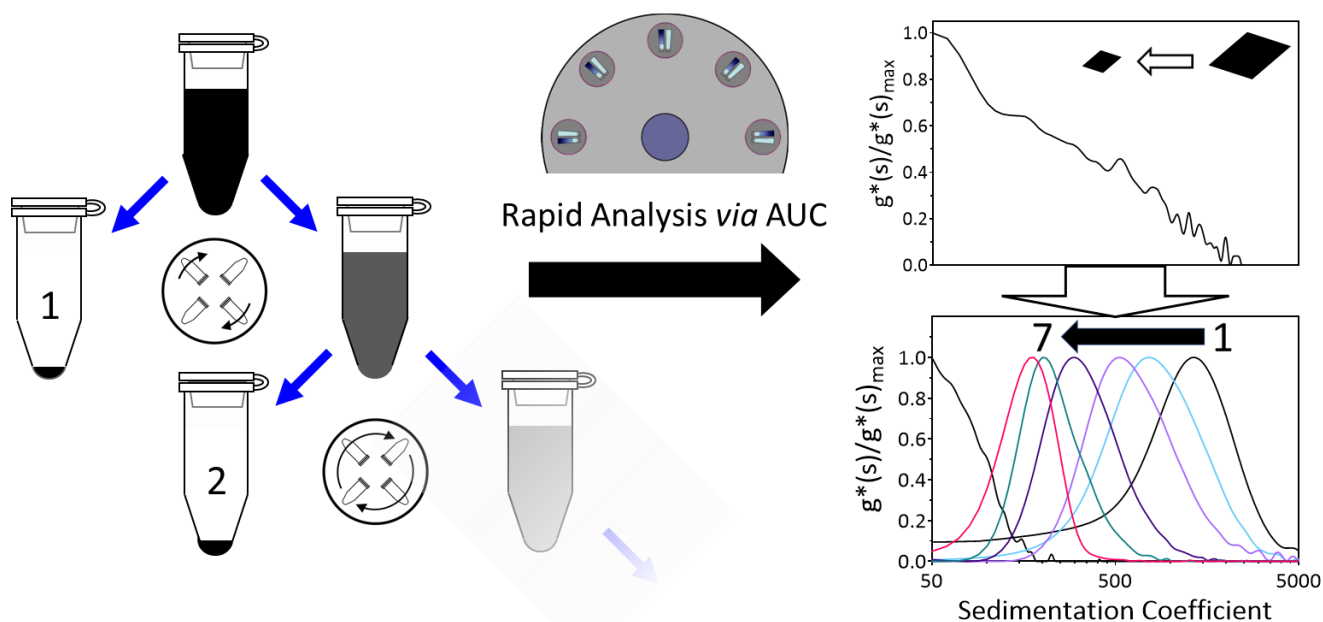
1. Lin, Z.; McCreary, A.; Briggs, N.; Subramanian, S.; Zhang, K.; Sun, Y.; Li, X.; Borys, N. J.; Yuan, H.; Fullerton-Shirey, S. K.; Chernikov, A.; Zhao, H.; McDonnell, S.; Lindenberg, A. M.; Xiao, K.; LeRoy, B. J.; Drndić, M.; Hwang, J. C. M.; Park, J.; Chhowalla, M.; Schaak, R. E.; Javey, A.; Hersam, M. C.; Robinson, J.; Terrones, M., *2D Mater.* **2016**, *3* (4), 042001. DOI 10.1088/2053-1583/3/4/042001.
2. Coleman, J. N.; Lotya, M.; O'Neill, A.; Bergin, S. D.; King, P. J.; Khan, U.; Young, K.; Gaucher, A.; De, S.; Smith, R. J.; Shvets, I. V.; Arora, S. K.; Stanton, G.; Kim, H.-Y.; Lee, K.; Kim, G. T.; Duesberg, G. S.; Hallam, T.; Boland, J. J.; Wang, J. J.; Donegan, J. F.; Grunlan, J. C.; Moriarty, G.; Shmeliov, A.; Nicholls, R. J.; Perkins, J. M.; Grievson, E. M.; Theuwissen, K.; McComb, D. W.; Nellist, P. D.; Nicolosi, V., *Science* **2011**, *331* (6017), 568. DOI 10.1126/science.1194975.
3. Backes, C.; Abdelkader, A. M.; Alonso, C.; Andrieux-Ledier, A.; Arenal, R.; Azpeitia, J.; Balakrishnan, N.; Banszerus, L.; Barjon, J.; Bartali, R.; Bellani, S.; Berger, C.; Berger, R.; Ortega, M. M. B.; Bernard, C.; Beton, P. H.; Beyer, A.; Bianco, A.; Bøggild, P.; Bonaccorso, F.; Barin, G. B.; Botas, C.; Bueno, R. A.; Carriazo, D.; Castellanos-Gomez, A.; Christian, M.; Ciesielski, A.; Ciuk, T.; Cole, M. T.; Coleman, J.; Coletti, C.; Crema, L.; Cun, H.; Dasler, D.; De Fazio, D.; Díez, N.; Drieschner, S.; Duesberg, G. S.; Fasel, R.; Feng, X.; Fina, A.; Forti, S.; Galiotis, C.; Garberoglio, G.; García, J. M.; Garrido, J. A.; Gibertini, M.; Götzhäuser, A.; Gómez, J.; Greber, T.; Hauke, F.; Hemmi, A.; Hernandez-Rodriguez, I.; Hirsch, A.; Hodge, S. A.; Huttel, Y.; Jepsen, P. U.; Jimenez, I.; Kaiser, U.; Kaplas, T.; Kim, H.; Kis, A.; Papagelis, K.; Kostarelos, K.; Krajewska, A.; Lee, K.; Li, C.; Lipsanen, H.; Liscio, A.; Lohe, M. R.; Loiseau, A.; Lombardi, L.; Francisca López, M.; Martin, O.; Martín, C.; Martínez, L.; Martin-Gago, J. A.;

- Ignacio Martínez, J.; Marzari, N.; Mayoral, Á.; McManus, J.; Melucci, M.; Méndez, J.; Merino, C.; Merino, P.; Meyer, A. P.; Miniussi, E.; Miseikis, V.; Mishra, N.; Morandi, V.; Munuera, C.; Muñoz, R.; Nolan, H.; Ortolani, L.; Ott, A. K.; Palacio, I.; Palermo, V.; Parthenios, J.; Pasternak, I.; Patane, A.; Prato, M.; Prevost, H.; Prudkovskiy, V.; Pugno, N.; Rojo, T.; Rossi, A.; Ruffieux, P.; Samorì, P.; Schué, L.; Setijadi, E.; Seyller, T.; Speranza, G.; Stampfer, C.; Stenger, I.; Strupinski, W.; Svirko, Y.; Taioli, S.; Teo, K. B. K.; Testi, M.; Tomarchio, F.; Tortello, M.; Treossi, E.; Turchanin, A.; Vazquez, E.; Villaro, E.; Whelan, P. R.; Xia, Z.; Yakimova, R.; Yang, S.; Yazdi, G. R.; Yim, C.; Yoon, D.; Zhang, X.; Zhuang, X.; Colombo, L.; Ferrari, A. C.; Garcia-Hernandez, M., *2D Mater.* **2020**, *7* (2), 022001. DOI 10.1088/2053-1583/ab1e0a.
4. Kang, J.; Sangwan, V. K.; Wood, J. D.; Hersam, M. C., *Acc. Chem. Res.* **2017**, *50* (4), 943-951. DOI 10.1021/acs.accounts.6b00643.
  5. Han, J. H.; Kwak, M.; Kim, Y.; Cheon, J., *Chem. Rev.* **2018**, *118* (13), 6151-6188. DOI 10.1021/acs.chemrev.8b00264.
  6. Chae, D.-H.; Utikal, T.; Weisenburger, S.; Giessen, H.; Klitzing, K. v.; Lippitz, M.; Smet, J., *Nano Lett.* **2011**, *11* (3), 1379-1382. DOI 10.1021/nl200040q.
  7. Ott, S.; Wolff, N.; Rashvand, F.; Rao, V. J.; Zaumseil, J.; Backes, C., *Chem. Mater.* **2019**, *31* (20), 8424-8431. DOI 10.1021/acs.chemmater.9b02336.
  8. Synnatschke, K.; Cieslik, P. A.; Harvey, A.; Castellanos-Gomez, A.; Tian, T.; Shih, C.-J.; Chernikov, A.; Santos, E. J. G.; Coleman, J. N.; Backes, C., *Chem. Mater.* **2019**, *31* (24), 10049-10062. DOI 10.1021/acs.chemmater.9b02905.
  9. Synnatschke, K.; Shao, S.; van Dinter, J.; Hofstetter, Y. J.; Kelly, D. J.; Grieger, S.; Haigh, S. J.; Vaynzof, Y.; Bensch, W.; Backes, C., *Chem. Mater.* **2019**, *31* (21), 9127-9139. DOI 10.1021/acs.chemmater.9b03468.
  10. Hu, C.-X.; Shin, Y.; Read, O.; Casiraghi, C., *Nanoscale* **2021**, *13* (2), 460-484. DOI 10.1039/D0NR05514J.
  11. Reina, A.; Son, H.; Jiao, L.; Fan, B.; Dresselhaus, M. S.; Liu, Z.; Kong, J., *J. Phys. Chem. C* **2008**, *112* (46), 17741-17744. DOI 10.1021/jp807380s.
  12. Li, Z.; Young, R. J.; Backes, C.; Zhao, W.; Zhang, X.; Zhukov, A. A.; Tillotson, E.; Conlan, A. P.; Ding, F.; Haigh, S. J.; Novoselov, K. S.; Coleman, J. N., *ACS Nano* **2020**, *14* (9), 10976-10985. DOI 10.1021/acsnano.0c03916.
  13. Halbig, C. E.; Nacken, T. J.; Walter, J.; Damm, C.; Eigler, S.; Peukert, W., *Carbon* **2016**, *96*, 897-903. DOI <https://doi.org/10.1016/j.carbon.2015.10.021>.
  14. Backes, C.; Campi, D.; Szydłowska, B. M.; Synnatschke, K.; Ojala, E.; Rashvand, F.; Harvey, A.; Griffin, A.; Sofer, Z.; Marzari, N.; Coleman, J. N.; O'Regan, D. D., *ACS Nano* **2019**, *13* (6), 7050-7061. DOI 10.1021/acsnano.9b02234.
  15. Yomogida, Y.; Liu, Z.; Ichinose, Y.; Yanagi, K., *ACS Omega* **2018**, *3* (8), 8932-8936. DOI 10.1021/acsomega.8b00745.
  16. Khan, U.; O'Neill, A.; Porwal, H.; May, P.; Nawaz, K.; Coleman, J. N., *Carbon* **2012**, *50* (2), 470-475. DOI <https://doi.org/10.1016/j.carbon.2011.09.001>.
  17. Backes, C.; Szydłowska, B. M.; Harvey, A.; Yuan, S.; Vega-Mayoral, V.; Davies, B. R.; Zhao, P.-I.; Hanlon, D.; Santos, E. J. G.; Katsnelson, M. I.; Blau, W. J.; Gadermaier, C.; Coleman, J. N., *ACS Nano* **2016**, *10* (1), 1589-1601. DOI 10.1021/acsnano.5b07228.
  18. Backes, C.; Hanlon, D.; Szydłowska, B. M.; Harvey, A.; Smith, R. J.; Higgins, T. M.; Coleman, J. N., *J. Vis. Exp.* **2016**, (118), 54806. DOI 10.3791/54806.
  19. Kozlova, M. N.; Artemkina, S. B.; Podlipskaya, T. Y.; Nebogatikova, N. A.; Das, M. R.; Fedorov, V. E., *Russ. Chem. Bull.* **2017**, *66* (6), 963-968. DOI 10.1007/s11172-017-1839-z.
  20. Kajbafvala, M.; Farbod, M., *Journal of Colloid and Interface Science* **2018**, *527*, 159-171. DOI <https://doi.org/10.1016/j.jcis.2018.05.026>.
  21. Woods, M. B.; Beidaghi, M.; Davis, V. A., *Langmuir* **2024**, *40* (6), 2907-2917. DOI 10.1021/acs.langmuir.3c02851.

22. Livshits, M. A.; Khomyakova, E.; Evtushenko, E. G.; Lazarev, V. N.; Kulemin, N. A.; Semina, S. E.; Generozov, E. V.; Govorun, V. M., *Sci. Rep.* **2015**, *5* (1), 17319. DOI 10.1038/srep17319.
23. Mächtle, W.; Börger, L., *Analytical Ultracentrifugation of Polymers and Nanoparticles*. Springer: Heidelberg, Germany, **2006**; p 237.
24. Schuck, P., *Sedimentation Velocity Analytical Ultracentrifugation: Discrete Species and Size-Distributions of Macromolecules and Particles* 1st ed.; CRC Press: Boca Raton, FL, USA, **2016**; p 266.
25. Walter, J.; Nacken, T. J.; Damm, C.; Thajudeen, T.; Eigler, S.; Peukert, W., *Small* **2015**, *11* (7), 814-825. DOI 10.1002/smll.201401940.
26. Frank, U.; Drobek, D.; Sanchez-Iglesias, A.; Wawra, S. E.; Nees, N.; Walter, J.; Pflug, L.; Apeleo Zubiri, B.; Spiecker, E.; Liz-Marzan, L. M.; Peukert, W., *ACS Nano* **2023**, *17* (6), 5785-5798. DOI 10.1021/acsnano.2c12257.
27. Palaganas, J. O.; Palaganas, N. B.; Ramos, L. J. I.; David, C. P. C., *ACS Appl. Mater. Interfaces* **2019**, *11* (49), 46034-46043. DOI 10.1021/acscami.9b12071.
28. Ramírez-Soria, E.-H.; Bonilla-Cruz, J.; Flores-Amaro, M. G.; García, V. J.; Lara-Ceniceros, T. E.; Longoria-Rodríguez, F. E.; Elizondo, P.; Advincula, R. C., *ACS Appl. Mater. Interfaces* **2020**, *12* (43), 49061-49072. DOI 10.1021/acscami.0c13702.
29. de Moraes, A. C. M.; Obrzut, J.; Sangwan, V. K.; Downing, J. R.; Chaney, L. E.; Patel, D. K.; Elmquist, R. E.; Hersam, M. C., *Journal of Materials Chemistry C* **2020**, *8* (43), 15086-15091. DOI 10.1039/D0TC03309J.
30. Ghirlando, R.; Balbo, A.; Piszczek, G.; Brown, P. H.; Lewis, M. S.; Brautigam, C. A.; Schuck, P.; Zhao, H., *Anal. Biochem.* **2013**, *440* (1), 81-95. DOI <https://doi.org/10.1016/j.ab.2013.05.011>.
31. Ma, J.; Zhao, H.; Sandmaier, J.; Alexander Liddle, J.; Schuck, P., *Biophys. J.* **2016**, *110* (1), 103-112. DOI <https://doi.org/10.1016/j.bpj.2015.11.027>.
32. Schuck, P., *Biophys. J.* **2000**, *78* (3), 1606-1619. DOI [https://doi.org/10.1016/S0006-3495\(00\)76713-0](https://doi.org/10.1016/S0006-3495(00)76713-0).
33. Schuck, P.; Rossmanith, P., *Biopolymers* **2000**, *54* (5), 328-341. DOI [https://doi.org/10.1002/1097-0282\(20001015\)54:5<328::AID-BIP40>3.0.CO;2-P](https://doi.org/10.1002/1097-0282(20001015)54:5<328::AID-BIP40>3.0.CO;2-P).
34. Despotelis, K.; Pollard, A.; Clifford, C.; Paton, K. *Graphene and related 2D materials project 12 - Distribution of lateral size and thickness of few-layer graphene flakes using SEM and AFM*; **2022**.
35. van der Kooij, F. M.; Philipse, A. P.; Dhont, J. K. G., *Langmuir* **2000**, *16* (12), 5317-5323. DOI 10.1021/la991571b.
36. Holmqvist, P.; Meester, V.; Westermeier, F.; Kleshchanok, D., *The Journal of Chemical Physics* **2013**, *139* (8), 084905. DOI 10.1063/1.4818532.
37. Diaz-Arauzo, S.; Downing, J. R.; Tsai, D.; Trost, J.; Hui, J.; Donahue, K.; Antonopoulos, N.; Chaney, L. E.; Dunn, J. B.; Hersam, M. C., *Mater. Horiz.* **2024**, *11* (23), 5960-5971. DOI 10.1039/D4MH01205D.
38. Green, A. A.; Hersam, M. C., *J. Phys. Chem. Lett.* **2010**, *1* (2), 544-549. DOI 10.1021/jz900235f.
39. Fagan, J. A.; Becker, M. L.; Chun, J.; Hobbie, E. K., *Adv. Mater.* **2008**, *20* (9), 1609+. DOI 10.1002/adma.200702353.
40. Sun, X.; Luo, D.; Liu, J.; Evans, D. G., *ACS Nano* **2010**, *4* (6), 3381-3389. DOI 10.1021/nn1000386.
41. Maleski, K.; Ren, C. E.; Zhao, M.-Q.; Anasori, B.; Gogotsi, Y., *ACS Appl. Mater. Interfaces* **2018**, *10* (29), 24491-24498. DOI 10.1021/acscami.8b04662.
42. Green, A. A.; Hersam, M. C., *Nano Lett.* **2009**, *9* (12), 4031-4036. DOI 10.1021/nl902200b.
43. Kang, J.; Seo, J.-W. T.; Alducin, D.; Ponce, A.; Yacaman, M. J.; Hersam, M. C., *Nat. Commun.* **2014**, *5* (1), 5478. DOI 10.1038/ncomms6478.
44. Zhu, J.; Kang, J.; Kang, J.; Jariwala, D.; Wood, J. D.; Seo, J.-W. T.; Chen, K.-S.; Marks, T. J.; Hersam, M. C., *Nano Lett.* **2015**, *15* (10), 7029-7036. DOI 10.1021/acs.nanolett.5b03075.
45. Kang, J.; Sangwan, V. K.; Wood, J. D.; Liu, X.; Balla, I.; Lam, D.; Hersam, M. C., *Nano Lett.* **2016**, *16* (11), 7216-7223. DOI 10.1021/acs.nanolett.6b03584.
46. Schuck, P.; Zhao, H., *Sedimentation Velocity Analytical Ultracentrifugation: Interacting Systems*. CRC Press: Boca Raton, FL, USA, **2017**; p 297.

47. Brown, P. H.; Balbo, A.; Zhao, H.; Ebel, C.; Schuck, P., *PLoS One* **2011**, *6* (10), e26221. DOI 10.1371/journal.pone.0026221.
48. Fagan, J. A.; Zheng, M.; Rastogi, V.; Simpson, J. R.; Khripin, C. Y.; Silvera Batista, C. A.; Hight Walker, A. R., *ACS Nano* **2013**, *7* (4), 3373-87. DOI 10.1021/nn4002165.
49. Backes, C.; Paton, K. R.; Hanlon, D.; Yuan, S.; Katsnelson, M. I.; Houston, J.; Smith, R. J.; McCloskey, D.; Donegan, J. F.; Coleman, J. N., *Nanoscale* **2016**, *8* (7), 4311-4323. DOI 10.1039/C5NR08047A.
50. Lotya, M.; Rakovich, A.; Donegan, J. F.; Coleman, J. N., *Nanotechnology* **2013**, *24* (26), 265703. DOI 10.1088/0957-4484/24/26/265703.
51. Harvey, A.; Backes, C.; Boland, J. B.; He, X.; Griffin, A.; Szydłowska, B.; Gabbett, C.; Donegan, J. F.; Coleman, J. N., *Nat. Commun.* **2018**, *9* (1), 4553. DOI 10.1038/s41467-018-07005-3.
52. Chen, S.; Duan, J.; Vasileff, A.; Qiao, S. Z., *Angew. Chem. Int. Ed.* **2016**, *55* (11), 3804-3808. DOI 10.1002/anie.201600387.
53. Tay, D. M. Y.; Li, B. L.; Tan, E. S. L.; Loh, K. P.; Leong, D. T., *Adv. Funct. Mater.* **2018**, *28* (29), 1801622. DOI 10.1002/adfm.201801622.

## Table of Contents



Analytical ultracentrifugation (AUC) is used to characterize graphene dispersions fractionated by differential sedimentation (DS). AUC enables characterization of daughter fractions in native, and complex, solution environments, avoiding artifacts common to surface analysis methods, and herein allowing demonstration of improved separations by simple modifications to the DS cascade. AUC characterization could be particularly useful for dispersions with dispersants or from which solutes cannot be removed.